First-principles study of the mechanical and optical properties of amorphous hydrogenated silicon and silicon-rich silicon oxide

Robert J. Bondi, Sangheon Lee, and Gyeong S. Hwang[*]

Department of Chemical Engineering, University of Texas at Austin, Austin, Texas 78712, USA
(Received 3 October 2009; revised manuscript received 6 March 2010; published 14 May 2010)

We use first-principles density-functional theory (DFT) calculations to predict mechanical and optical property variation with composition for hydrogenated amorphous Si (a-Si:H) (at. % H=0, 5.9, 11.1, and 15.8) and a-SiO$_x$ (x=0, 0.5, 1.0, 1.5, and 2.0). A better understanding of the properties of a-Si:H and amorphous silicon oxide (a-SiO$_x$) is technologically important, particularly for photovoltaic and optoelectronic device applications, respectively. However, relatively little reliable property information is available for these amorphous materials except for the well-studied end-point cases of a-Si and a-SiO$_2$. Our DFT calculations within the generalized gradient approximation predict that addition of H to a-Si monotonically reduces the elastic modulus (Y) by 18% and bulk modulus (B) by 16% as H incorporation increases to 15.8 at. % in a-Si:H. Similarly, addition of O to a-Si monotonically reduces Y by 35% and B by 38% as x increases to 2.0 in a-SiO$_x$. Our optical spectra for the complex dielectric function, $\varepsilon(\omega)$, exhibit intensity reduction in the E_2 transition peak of Im$[\varepsilon(\omega)]$ and reduction in the low-frequency dielectric constant $\{\varepsilon_\mathrm{o}=\lim_{\omega\to0}\mathrm{Re}[\varepsilon(\omega)]\}$ as either H or O are added to a-Si while the a-SiO$_x$ spectra additionally resolve a vivid blueshift of both the fundamental absorption edge and E_2 transition energy as O content increases. Considering the large variation in reported experimental measurements and the limited availability of previous computational results, our property predictions provide valuable insight into the mechanical and optical behavior of a-Si:H and a-SiO$_x$ materials.

I. INTRODUCTION

The foundations for the use of amorphous semiconductors in photovoltaic and optoelectronic applications began in the 1960s when early work demonstrated that short-range order (SRO) sufficiently retained key optical properties present in crystalline semiconductors.[1] In an amorphous semiconductor, the disordered covalent network contains minor deviations in bond length and larger variations in bond angle relative to its counterpart crystalline lattice.[2] In the 1970s, Carlson and Wronski[3] reported the first feasible amorphous Si (a-Si) *p-i-n* solar cell using a-Si with radically reduced gap defect densities attributed to H compensation of dangling bonds. Hydrogenated a-Si (a-Si:H) is remarkably promising for solar applications because the redshifted absorption coefficient relative to crystalline Si (c-Si) could ultimately allow realization of inexpensive thin-film (≤ 1 μm) solar cells if the light-induced degradation of the Staebler-Wronski effect[4] (SWE) is circumvented. Recent experimental work has shown that mixed-phase materials, such as nanocrystalline Si (nc-Si) dispersed in a-Si:H, can potentially mitigate the reversible SWE.[5]

In recent years, nanostructure fabrication techniques have introduced the capability of growing nc-Si in Si-rich amorphous silicon oxide (a-SiO$_x$) matrices to produce flash memory[6] dielectrics and materials capable of light emission[7,8] via size-tunable photoluminescence and electroluminescence processes. While many suggest light emission from nc-Si embedded in a-SiO$_x$ is driven by quantum confinement, discrepancies in experimental results suggest other phenomena may also be influential, such as sensitive chemical functional groups and oxide defects that may be stabilized at the nc-Si/a-SiO$_x$ interface and size-dependent (curvature) interfacial strain energy. A variety of synthesis techniques have been reported to produce nc-Si embedded in a-SiO$_x$ including cosputtering of Si and SiO$_2$ and Si-ion implantation into SiO$_2$ thin films.[7] Regardless of fabrication technique, a recent theoretical study has suggested that the mechanism promoting nc-Si formation in a-SiO$_x$ is largely governed by suboxide penalty from incomplete O coordination.[9] At the present, relatively little reliable property information for a-SiO$_x$ ($0 < x < 2$) is available in comparison to the well-studied end-point cases of a-Si and a-SiO$_2$.

In this paper, we use established methods based on first-principles density-functional theory calculations to predict mechanical and optical properties for both a-Si:H and a-SiO$_x$ bulk materials. In particular, we evaluate various compositions of bulk a-Si:H (at. % H=0, 5.9, 11.1, and 15.8) and a-SiO$_x$ (x=0, 0.5, 1.0, 1.5, and 2.0) to demonstrate elastic and bulk moduli predictions. For the same matrix compositions, we also present the real and imaginary components of the complex dielectric function spectra $[\varepsilon(\omega)=\varepsilon'(\omega)+i\varepsilon''(\omega)]$, low-frequency dielectric constants (ε_o), and band gaps (E_g). Overall comparison of our results with previous experimental measurements and available theoretical studies shows reasonable agreement for a-Si and a-SiO$_2$, which have been heavily studied. Our mechanical and optical property predictions provide valuable characterization of property variation with composition for these technologically significant materials while simultaneously evaluating theoretical methodologies that are easily applicable to other materials.

II. COMPUTATIONAL FRAMEWORK

All atomic structures and properties reported herein were calculated using a plane-wave pseudopotential method within the generalized gradient approximation of Perdew and

TABLE I. Computed mechanical property summary by composition of a-Si:H and a-SiO$_x$ structures. Sample names quantify the constituent atomic species in each supercell. BZ sampling schemes using MP meshes are given for geometric optimization together with increased sampling schemes in () when optimized ionic positions were fixed. The average mass density over each sample count is given by $\boldsymbol{\rho}_m$. Y represents an average elastic modulus over all structures sampled, each of which is an average over the strain conditions evaluated. The uncertainty associated with each Y is the average standard deviation obtained from each sample. B represents analogous quantities for the bulk modulus.

Sample	Sample count	k-point mesh[a]	E_{cut} [b]	ρ_m (g/cm^3)	Y (GPa)	B (GPa)
			a-Si:H			
aSi64	3	$\alpha(\beta)$	γ	2.26	140.7 ± 8.1	74.5 ± 14.9
aSi64H4	4	$\alpha(\beta)$	γ	2.20	134.0 ± 18.1	70.9 ± 15.1
aSi64H8	5	$\alpha(\beta)$	γ	2.17	121.5 ± 7.8	67.9 ± 16.2
aSi64H12	5	$\alpha(\beta)$	γ	2.13	115.0 ± 10.5	62.4 ± 14.6
			a-SiO$_x$			
aSi64	3	$\alpha(\beta)$	γ	2.26	140.7 ± 8.1	74.5 ± 14.9
aSi64O32	4	$\Gamma(\alpha)$	λ	2.24	129.0 ± 8.6	66.9 ± 11.9
aSi64O64	4	$\Gamma(\alpha)$	λ	2.21	118.1 ± 12.1	63.1 ± 9.4
aSi64O96	4	$\Gamma(\alpha)$	λ	2.16	101.3 ± 13.6	56.6 ± 11.2
aSi48O96	3	$\Gamma(\alpha)$	λ	2.17	91.4 ± 19.6	46.0 ± 12.2

[a]$\Gamma = \Gamma$ point, $\alpha = (2 \times 2 \times 2)$, and $\beta = (3 \times 3 \times 3)$.
[b]$\gamma = 160$ eV and $\lambda = 350$ eV.

Wang (GGA-PW91) (Ref. [10]) to density-functional theory (DFT),[11] as implemented in the Vienna *ab initio* simulation package (VASP).[12] We employed Vanderbilt-type ultrasoft pseudopotentials[13] to represent the interaction between ion cores and valence electrons in mechanical property predictions and projector-augmented wave (PAW) pseudopotentials[14] for the computation of optical properties. The PAW methodology, which is, in principle, an all-electron frozen-core approach that represents exact valence wave functions, was used for optical property calculations to ensure enhanced representation of electronic transitions.

A. Mechanical properties

For mechanical property calculations, the kinetic-energy cutoffs (E_{cut}) for the plane-wave basis set and the Monkhorst-Pack (MP) grids for Brillouin-zone (BZ) sampling are summarized in Table I. Geometric optimization was run on all structures until residual forces had converged within 5×10^{-2} eV/Å tolerance. With optimized ionic positions fixed, total energies were reevaluated using increased k-point sampling as indicated in Table I. Adequate BZ sampling was determined for various compositions by increasing k-point sampling until total-energy convergence was achieved.

The elastic (or Young's) modulus (Y) was calculated by computing forces and stresses from total-energy (E) data using the following relationships:

$$F_x = \left. \frac{\partial E_x}{\partial x} \right|_{x=\varepsilon}, \tag{1}$$

$$\sigma_{xx} = \frac{F_x}{A}, \tag{2}$$

$$Y = \frac{\sigma_{xx}}{\varepsilon}. \tag{3}$$

Forces along a given direction (F_x) were calculated for each strain condition (ε) using second-order numerical derivatives in Eq. (1), normal stresses (σ_{xx}) were subsequently evaluated with Eq. (2) (A represents the supercell face area in the x direction), and ultimately Young's modulus is obtained from Eq. (3) as the ratio of stress to strain in the x direction. To provide adequate statistical sampling of Y for each structure sample, Y was evaluated at each condition for $-5\% \leq \varepsilon \leq 5\%$ at 0.5% intervals using a custom Perl script to manage numerous VASP simulations. To ensure a stress-free state occurs at strain-free conditions, a small, systematic correction (on the order of 1 GPa) was generally required for each structure and applied to all stress calculations.

The bulk modulus (B), which is the three-dimensional analog of Y, can be calculated from total-energy data as

$$B = V \left. \frac{\partial^2 E}{\partial V^2} \right|_{V=V_i} = \frac{\dfrac{\partial E}{\partial V}}{\dfrac{\Delta V}{V_o}} = \frac{\text{volumetric stress}}{\text{volumetric strain}}, \tag{4}$$

where V_o is the equilibrium cell volume, $\varepsilon_v = \Delta V / V_o$ is an arbitrary volumetric strain, and V_i is the cell volume at an arbitrary ε_v. The work of Mehl[15] provides a similar computational approach to calculate B, except $E(V_i)$ data is mathematically fit to an isothermal equation of state described by

Birch[16] with subsequent analytic differentiation, whereas our method substitutes the approximation inherent in fitting with the approximation inherent in a statistical approach. Similar to our treatment of Y, B was evaluated at each condition for $-5\% \leq \varepsilon_v \leq 5\%$ at 0.5% intervals and corrections generally <1 GPa were applied to enforce correspondence between stress-free states and strain-free conditions.

While both Y and B were evaluated at 21 strain conditions per sample $[-5\% \leq y \leq 5\%$ ($y = \varepsilon, \varepsilon_v$ at 0.5% intervals)], the mechanical responses nearest strain-free conditions were systematically poorly behaved; consequently, our reported values in Table I represent the remaining 16 strain conditions per sample following omission of the data range $-1\% \leq y \leq 1\%$ ($y = \varepsilon, \varepsilon_v$). Additional mechanical properties, such as Poisson's ratio (ν) and shear modulus (G), can be calculated once Y and B are known because only two of these four quantities are independent in isotropic materials.[17]

B. Optical properties

For optical property calculations, the cutoff energies employed with PAW pseudopotentials were 250 eV and 300 eV for a-Si/a-Si:H and a-SiO$_x$ ($x > 0$) systems, respectively. Note that the same DFT calculation conditions were used for a-Si and a-Si:H, unless noted otherwise. We utilized a four-step procedure to compute the complex-frequency-dependent dielectric function with VASP following the general theoretical framework described by Adolph *et al.*[18] and cited in other recent computational studies for other material systems.[19–22] This calculation procedure is based on the independent-particle approximation so quasiparticle self-energy corrections, local-field effects, and excitonic contributions are neglected.

First, the ionic positions in each structure sample were optimized using the same force convergence criterion as the mechanical property calculations and the same BZ sampling schemes shown in Table I. Second, the charge-density distribution was obtained with $5 \times 5 \times 5$ and $3 \times 3 \times 3$ k-point meshes for a-Si:H and a-SiO$_x$, respectively. Third, the frequency-dependent dielectric matrix was calculated from the optimized charge-density distribution using the tetrahedron method[12] and 200 conduction bands for each composition (which was found sufficient to sample transition energies across the range of supercell sizes investigated). Finally, the OPTICS code of Furthmüller[23] was used to obtain both the imaginary (ε'') and real (ε') parts of $\varepsilon(\omega)$. The imaginary part of $\varepsilon(\omega)$ (in atomic units) is computed by summation over the frequency-dependent dielectric matrix elements in these isotropic materials using

$$\text{Im}[\varepsilon(\omega)] = \varepsilon''(\omega)$$
$$= \frac{4\pi^2}{\Omega \omega^2} \sum_{i \in \text{VB}, j \in \text{CB}} \sum_{\mathbf{k}} w_{\mathbf{k}} |p_{ij}|^2 \delta(\varepsilon_{\mathbf{k}j} - \varepsilon_{\mathbf{k}i} - \omega), \quad (5)$$

where Ω is the unit-cell volume, VB represents the valence band, CB represents the conduction band, $w_{\mathbf{k}}$ is a weighting associated with a k-point $\mathbf{k}$, and $\varepsilon_{\mathbf{k}n}$ represent energy levels in their respective bands.[19] Transition matrix elements in Eq. (5) are represented by $p_{ij} = \langle \mathbf{k}_i | \hat{p} | \mathbf{k}_j \rangle$, where the $|\mathbf{k}_n\rangle$ are

Bloch-state wave functions with momentum $\mathbf{k}$. We used the longitudinal form[12,19,24] of the dielectric matrix in our VASP calculations throughout this work. When the imaginary part of $\varepsilon(\omega)$ is known for all photon energies, application of the Kramers-Kronig transformation (in atomic units),

$$\text{Re}[\varepsilon(\omega)] = \varepsilon'(\omega) = 1 + \frac{2}{\pi} \mathbf{P} \int_0^\infty \frac{\omega' \varepsilon''(\omega')}{\omega'^2 - \omega^2} d\omega', \quad (6)$$

where $\mathbf{P}$ represents the principal integral value, allows subsequent evaluation of the real component of $\varepsilon(\omega)$. We found that calculations of optical transitions up to 20 eV was sufficient to obtain the key features in the dielectric function spectra. With $\varepsilon(\omega)$ determined, it is relatively straightforward to derive other linear optical properties including refractive index, reflectivity, absorption coefficient, optical conductivity, and electron energy-loss spectra.[25,26]

C. Structure generation

We constructed largely defect-free a-SiO$_x$ and a-Si:H structures using an approach described in further detail by Yu *et al.*[9] that employs continuous random network model-based Metropolis Monte Carlo (MMC) sampling with Keating-type potentials. To sample the structural variation present in the amorphous samples, three to five independent structures were evaluated for each stoichiometric composition in our study. Figure 1 shows the lowest-energy configuration for each composition investigated, while Table I summarizes supercell composition and size, sample quantity, and density.

Figures 2 and 3 show the radial distribution function (RDF) of each composition in our study to provide a metric for comparison of SRO in our amorphous structures. Each subplot represents the average SRO of all samples of a given composition. In Fig. 2, the Si-H peak location is consistent with the reported[27] Si-H bond length of 1.48 Å. In the generation of our a-Si:H structures, care was taken in the initial MMC seeding to homogenize the H atoms to inhibit the occurrence of molecular hydrogen. Since the H$_2$ bond length is 0.74 Å,[28] our RDF data in Fig. 2 indeed shows that H$_2$ is absent in our structures. Statistical analysis of bond angles ($\theta_{\text{Si-Si-Si}}$ and $\theta_{\text{Si-Si-H}}$) in our structures shows a trend for both the average and standard deviation to increase slowly as H content increases.

In Fig. 3, the first nearest-neighbor peak of Si-Si, typically near 2.34 Å in a-Si,[27] decays away while the Si-O and O-O peaks intensify as x increases in a-SiO$_x$. The sharpest peak representing the Si-O bond occurs near 1.6 Å, which is typical in vitreous SiO$_2$.[29] Like the a-Si:H structures, statistical analysis of bond angles ($\theta_{\text{Si-Si-Si}}$, $\theta_{\text{O-Si-O}}$, $\theta_{\text{Si-O-Si}}$, and $\theta_{\text{Si-Si-O}}$) shows a trend for increasing average bond angle as O content increases. The Si-O-Si bond angle is an important metric for characterizing amorphous silica. The average $\theta_{\text{Si-O-Si}}$ for our three a-SiO$_2$ samples is $150.5° \pm 10.9°$, which is in excellent agreement with measurements derived from NMR spectra of $151° \pm 11°$.[30] Analysis of the ring-size distribution shows that six-membered rings are preferred across the entire a-SiO$_x$ composition range but the distribution spreads as O content is increased.
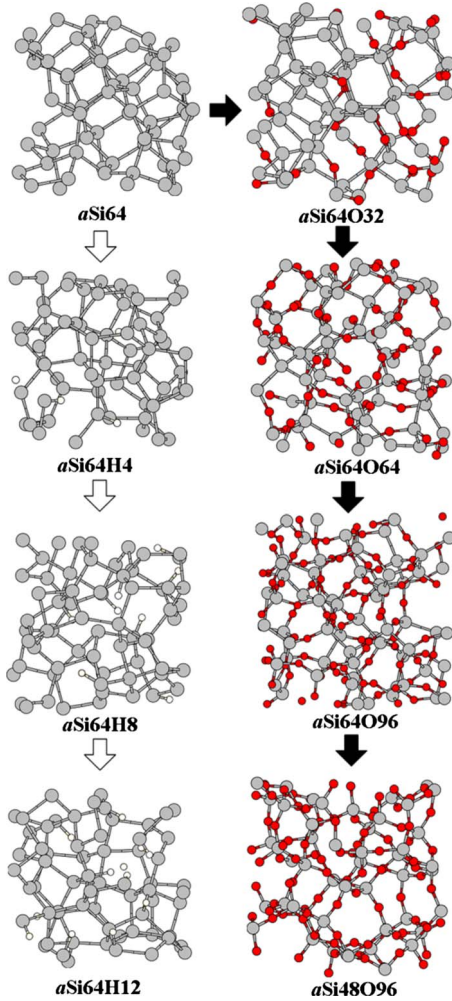
FIG. 1. (Color online) Amorphous configurations of various compositions of a-Si:H and a-SiO$_x$ constructed from a-Si. White and black block arrows denote increasing H and O content, respectively. Configuration names quantify the constituent atomic species in each sample supercell. Silicon, oxygen, and hydrogen atoms are represented by gray (large), red (medium), and white (small) spheres, respectively.

To accommodate the unique structural topology of each sample, we performed volume relaxation using DFT on each cubic supercell to determine the equilibrium volume and density of every structure. We found that equilibrium volume determination from sample-specific volume relaxation, rather than a fixed volume determined from experimental densities, was more beneficial in producing expected mechanical responses in this computational framework. Consistent with experimental results, the densities of our lowest-energy structures for a-Si and a-SiO$_2$ show the best agreement with published densities of 2.30 ± 0.01 (Ref. 31) and 2.2 g/cm^3 (Ref. 32), respectively. For further structural comparison, we obtained qualitatively similar electronic density of states for our aSi64H8 samples as reported structures of identical composition prepared using molecular-dynamics simulations in Ref. 33.
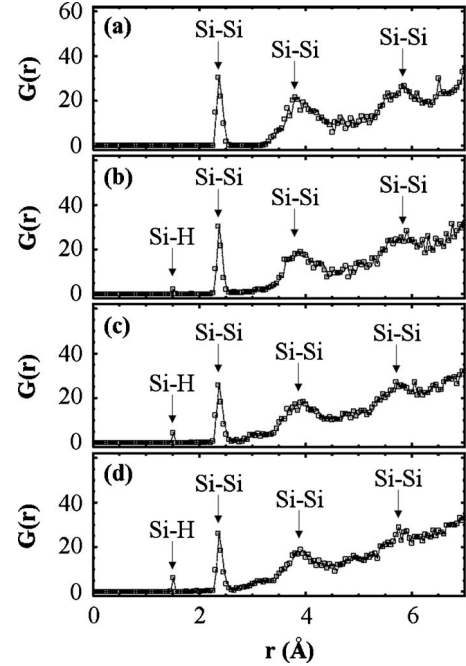

FIG. 2. Radial distribution functions characterizing the amorphous structure of (a) aSi64, (b) aSi64H4, (c) aSi64H8, and (d) aSi64H12 compositions of a-Si:H. Each plot represents the bond topology of all samples of that composition. Significant peaks are annotated by the corresponding interaction pair represented.

III. RESULTS AND DISCUSSION

A. Mechanical properties

Table I provides a summary of our mechanical property calculations over 35 total amorphous samples studied representing eight different compositions of a-Si:H and a-SiO$_x$ matrices. For the supercell sizes employed, it is not possible to achieve an ideally random sample of disordered bond topology, so we compensate by sampling multiple independent structures at various strain conditions. Standard deviations are provided with all calculated moduli to show the inherent variation that occurs when sampling small amorphous structures.

1. a-Si:H

From Table I, our calculations show a trend for the elastic modulus (Y) to decrease in a-Si:H materials as H content increases and density decreases. Y decreases from 140.7 to 115.0 GPa as H content increases from 0 to 15.8 at. %. Previous experimental results are varied for Y dependence on H content. Kuschnereit *et al.*[2] deposited both laser and plasma chemical vapor deposition (CVD) a-Si:H films and observed Y to reach a maximum of 134 ± 5 GPa at 10 at. % H, then sharply decrease with increasing H content. We see a similar Y of 121.5 GPa at 11.1 at. % H, but instead embedded in a monotonically decreasing trend with increasing H content. Kuschnereit *et al.* acknowledged both evidence of hydride polymerization for the highest H-content films and the simultaneous sharp decrease in density suggesting void formation as aspects likely unique to their CVD processes.
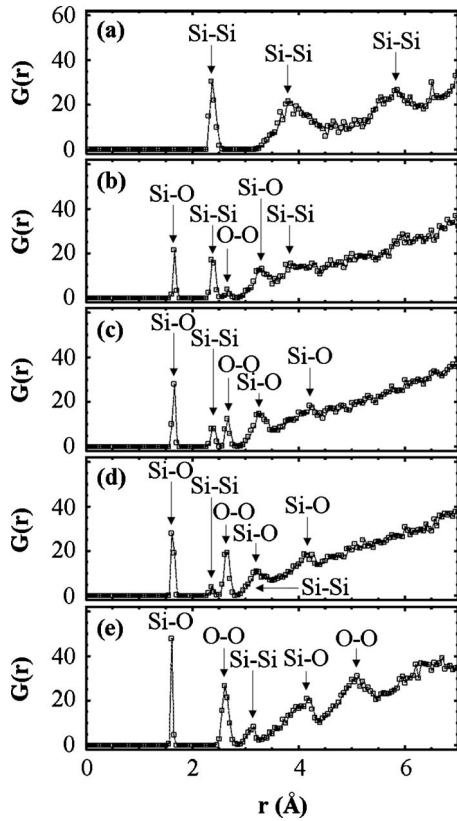
FIG. 3. Radial distribution functions characterizing the amorphous structure of (a) aSi64, (b) aSi64O32, (c) aSi64O64, (d) aSi64O96, and (e) aSi48O96 compositions of a-SiO$_x$. Each plot represents the bond topology of all samples of that composition. Significant peaks are annotated by the corresponding interaction pair represented.

In a different study, Jiang *et al.*[34] studied a-Si:H films deposited by rf sputtering and show a consistent decrease in Y from 100 GPa near 1 at. % H to 55 GPa near 17 at. % H. While their monotonically decreasing Y trend is similar to our results, they also show $Y \approx 105$ GPa for Si(111), which is lower than expected (Brantley[35] shows Y is 168.9 GPa on Si{111}). In addition, Jiang *et al.* acknowledged holes in the surface morphologies of their films which we think suggests void incorporation and consequent reduction in Y. We believe that our results deviate from these experimental studies because both the H distribution and void fraction in the deposited a-Si:H films is likely less homogeneous than our model atomic structure samples.

Our calculations also predict a trend for the bulk modulus to decrease as H incorporation in a-Si:H increases. B decreases from 74.5 to 62.4 GPa with increasing H content from 0 to 15.8 at. %, consistent with previous B experimental results [75–109 GPa for a-Si (Refs. 31 and 36) and 59 GPa for films with ~10% H (Ref. 37)]. This wide range of B (75–109 GPa) in a-Si from the work of Szabadi *et al.*[31] was determined using surface acoustic wave and Rutherford backscattering spectroscopies on amorphized Si layers in implanted c-Si. Their property summary provides a good example of the variation in amorphous material properties attributable to changes in implant dose, implant energy, and annealing parameters and also shows that both Y and B decrease as a-Si film density decreases.

In order to justify the three to five sample sizes used at each composition, we generated and evaluated mechanical properties for additional samples of both aSi64 and aSi64H12 structures. For aSi64, we increased the sample count from three to ten. As a result, Y decreased from 140.7 to 139.0 GPa and B increased from 74.5 to 75.6 GPa. This represents a 1.2% and 1.5% change in Y and B, respectively. For aSi64H12, we increased the sample count from 5 to 12. As a result, Y decreased from 115.0 to 114.8 GPa and B increased from 62.4 to 63.4 GPa. This represents a 0.3% and 1.6% change in Y and B, respectively. In our effort to balance calculation accuracy and computational requirements, we feel that the small percent change in our moduli predictions resulting from seven additional samples of aSi64 and aSi64H12 justifies our three to five sample count criterion in this work, particularly in our objective of identifying property changes as a function of composition.

2. a-SiO$_x$

Our calculations also show a clear trend for Y to decrease in a-SiO$_x$ as O content increases and density generally decreases. Our DFT-GGA calculations predict $Y = 140.7$ GPa and 91.4 GPa for a-Si and a-SiO$_2$, respectively. Experimentally measured Y values for a-Si range from 125 (Ref. 31) to 167 GPa.[38] For a-SiO$_2$, experimental Y measurements include 70 (Ref. 39) to 73 GPa (Ref. 40) in bulk silica, 76.6 ± 7.2 GPa (Ref. 41) for a-SiO$_2$ nanowires (independent of wire diameter), and values as large as 144 GPa have been reported in films deposited by plasma-enhanced chemical vapor deposition.[42]

Similarly, we observe a distinct trend for B to decrease in a-SiO$_x$ with increasing O content and decreasing density. Our predicted values of $B = 74.5$ GPa and 46.0 GPa in a-Si and a-SiO$_2$, respectively, are in good agreement with previous computational results [75 GPa for a-Si (Ref. 43) and 37 GPa for a-SiO$_2$ (Ref. 44)] and reasonable agreement with results determined from experimental studies [75–109 GPa for a-Si (Refs. 31 and 36) and 33.3 GPa for a-SiO$_2$ (Ref. 39)].

A limited amount of experimental information has been reported on the mechanical properties of amorphous silicon monoxide (a-SiO$_x$, $x = 1$) thin films. The work of Hoffman *et al.*[45] produced a-SiO$_x$ ($0.9 \leq x \leq 1.0$) films through various evaporative deposition techniques and Young's modulus measurements using a nanotensilometer. They reported Y to vary between 53 and 75 GPa, which suggests that Y for a-SiO is actually softer than either a-Si or a-SiO$_2$ and smaller than our computed Y of 118 GPa for a-SiO. However, they also acknowledged that the bulk film density (2.13 g/cm^3) used to calculate Y could be a likely source of variation in their reported values and further detailed that evaporative deposition can yield a-SiO films with densities varying from 1.51 to 2.15 g/cm^3. Furthermore, we suspect their assumed bulk density applied to all samples lowers the Y for their films. For comparison, the average density of our a-SiO samples is 2.21 g/cm^3, which is intermediate to the densities of our a-Si and a-SiO$_2$ samples. As previously described, we optimized the volume and density of every structure sample

and suspect this is the primary reason we found a higher Y for a-SiO.

3. Structural contributions to moduli

From the moduli synopsis in Table I, it is apparent that addition of either H or O to a-Si tends to reduce or soften both Y and B. Fundamentally, we can relate this observed property behavior to changes in atomic network connectivity. For example, a complete covalent network for Si only occurs in pure c-Si and Y along $\langle 110 \rangle$ directions within $\{100\}$ planes is 168.9 GPa.[35] In a-Si, disorder reduces the interconnectivity among Si atoms, the mean coordination number correspondingly falls below 4 and Y drops to 140.7 GPa (Table I). O incorporation in a-Si further reduces atomic connectivity because each O is a twofold-coordinated flexible linkage in the network rather than the more rigid fourfold-coordinated linkage of each Si in a-Si. As a result, bond-angle distortion in a-SiO$_x$ preferentially occurs at bond angles subtended by O atoms, not Si atoms. Similarly, H incorporation in a-Si increases the atomic network flexibility because every Si-H bond formed effectively severs covalent network interconnection. Decreased atomic network connectivity also correlates with a general reduction in density of a-Si as either H or O content is increased.

Variations in mechanical properties obtained via experiment are related to a number of factors including deposition process and conditions, annealing procedure, measurement technique, film density, material homogeneity, and sample purity. In our first-principles approach, the biggest source of property variation, particularly within the same composition, is likely attributable to limited sampling of the ideally random bond topology. We expect that the standard deviations in our reported moduli could be reduced through a better statistical sampling of the amorphous network by either increased sample counts (intersample variance reduction) and/or larger supercells (intrasample variance reduction).

B. Optical properties

Figures 4 and 5 show the optical spectra we obtained through calculation of the dielectric function for all compositions of a-Si:H and a-SiO$_x$ considered in our study. As typically seen in amorphous systems, the absence of long-range order and k-point conserving transitions smoothes out the optical response and washes away many of the characteristic transition edges and peaks exhibited by crystalline semiconductor spectra.[18,46] The major features that remain to distinguish among the amorphous samples are the fundamental absorption edge (E_0) and asymmetric main absorption peak (E_2) in Im$[\varepsilon(\omega)]$ and the transition energy of anomalous dispersion and dielectric constant (ε_o) evident in Re$[\varepsilon(\omega)]$. These key spectral features are also sensitive to material phase. For example, $\varepsilon_o = 11.9$ in c-Si (Ref. 1), while amorphization changes ε_o to ~ 16 in a-Si.[46] Similarly, $\varepsilon_o = 4.6$ in c-SiO$_2$ (α-quartz $\parallel$ to optical z axis[47]), while amorphization changes ε_o to 3.9 in a-SiO$_2$ (thermal oxide thin film[40]).

Figure 6 provides our DFT-calculated Im$[\varepsilon(\omega)]$ spectra for c-Si and c-SiO$_2$ (α-quartz) for comparison with their amorphous counterparts. Our c-Si spectra [Fig. 6(a)] is simi-
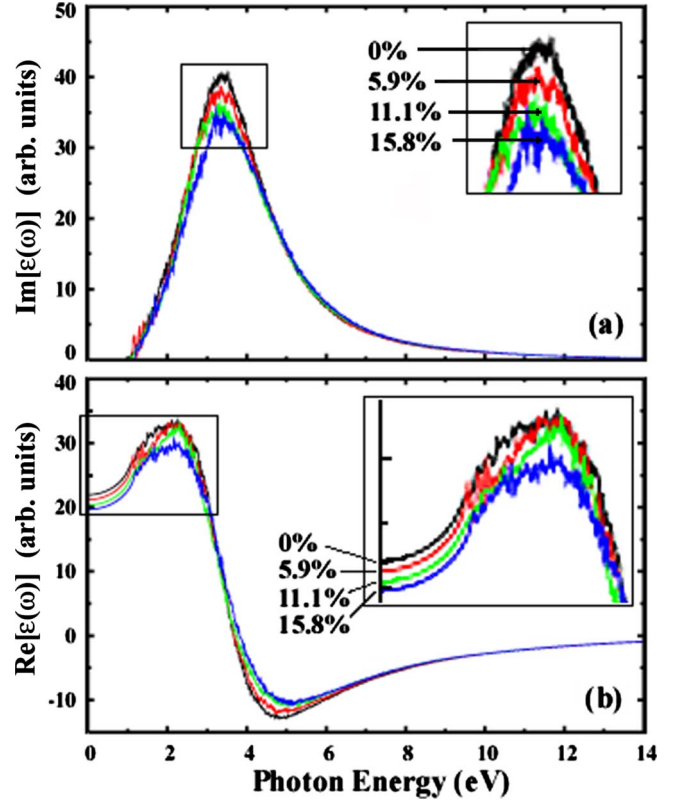

FIG. 4. (Color online) (a) Imaginary and (b) real parts of the complex dielectric function spectra for a-Si:H computed from DFT-GGA calculations. The spectra are annotated by at. % H. For each composition, only the lowest-energy structure is represented in the spectra. The insets provided illustrate the sequence of constituent spectra.

lar to that reported by Adolph *et al.*[18] and provides a classic example for introduction of important nomenclature in Im$[\varepsilon(\omega)]$ spectra. The onset of Im$[\varepsilon(\omega)]$ intensity in the low-energy region is often termed the fundamental absorption edge or E_0 transition. Im$[\varepsilon(\omega)]$ rises to an asymmetric peak (E_1) just above the absorption edge from transitions occurring along $\langle 111 \rangle$ directions in the BZ. The Im$[\varepsilon(\omega)]$ spectra typically reach a maximum at a characteristic energy called the E_2 transition, which is associated with transitions occurring over a large region of the BZ. Note that the well-known DFT band-gap underestimation in our GGA independent-particle calculations is manifested as spectral redshifting to lower energies, so our results should not be compared directly to experiments without proper adjustment of transition energies. Our c-SiO$_2$ spectra [Fig. 6(b)] is reasonably similar to that shown in Refs. 26 and 48 for α-quartz. The details of the electronic structure of c-SiO$_2$, even from experimental results, is often a bit ambiguous in the literature because of measurement difficulties associated with the formation of excitons that obscure accurate determination of the band gap and the persistence of crystal defects.[26]

1. a-Si:H

As shown in Fig. 4(a), the shape of Im$[\varepsilon(\omega)]$ incrementally transitions as the H content increases in a-Si:H. In par-
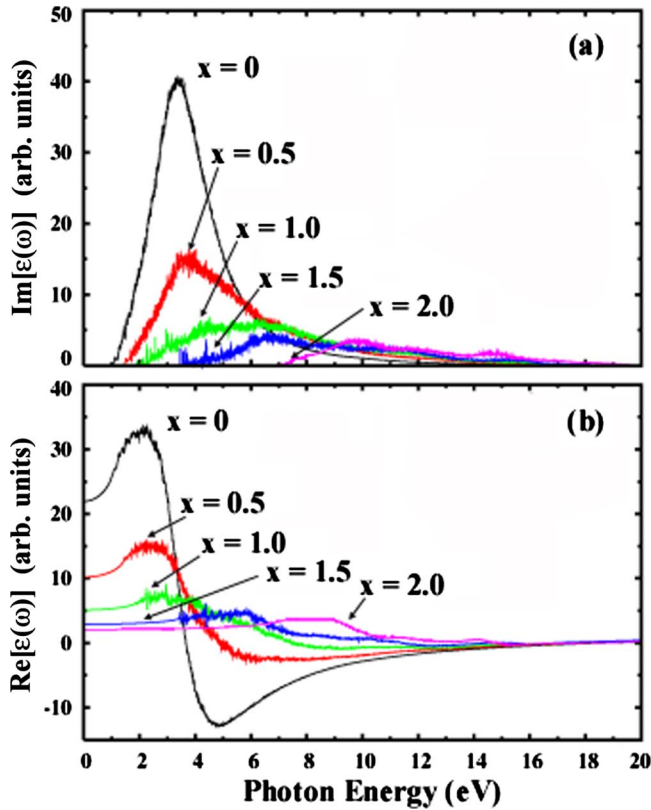
FIG. 5. (Color online) (a) Imaginary and (b) real parts of the complex dielectric function spectra for a-SiO$_x$ computed from DFT-GGA calculations. The spectra are annotated according to O stoichiometry (x) relative to Si. For each composition, only the lowest-energy structure is represented in the spectra.

ticular, the reduction in intensity of the main E_2 absorption peak, which occurs between 3 and 4 eV, is evident and consistent with experimentally-derived spectra.[46,49] In the Re$[\varepsilon(\omega)]$ spectra of Fig. 4(b), we observe a subtle broadening in the anomalous dispersion region that coincides with incremental reduction in ε_o as H incorporation increases. Decreasing spectral peak intensities and decreasing ε_o are observed for a-Si:H as H increases, which correlates with an increasing optical gap.[46] Experimental results[46] also confirm increasing H content lowers ε_o in a-Si:H.

Feng et al.[49] report Im$[\varepsilon(\omega)]$ spectra for a-Si:H films of variable H content grown by dc magnetron sputtering and measured with spectroscopic ellipsometry. Their spectra exhibits a similar reduction in E_2 peak intensity like we see in Fig. 4(a), as well as the expected blueshift of the E_2 peak as H content increases that is not readily apparent in our results. The expected blueshift of E_2 is easier to see in the results of Feng et al. partly because they examined films up to 24 at. % H. Despite the limitations of our DFT calculation methods, the E_2 transition energy for our unhydrogenated a-Si sample (3.4 eV) is surprisingly similar to the results of Feng et al. (3.60 eV). To produce their Im$[\varepsilon(\omega)]$ spectra from ellipsometric data, they made several assumptions that potentially affect their results: (1) 50% void fraction for estimation of the film surface-layer roughness, (2) film morphologies identical to those from previous experiments, and (3) validity of the effective-medium approximation[50] to de-
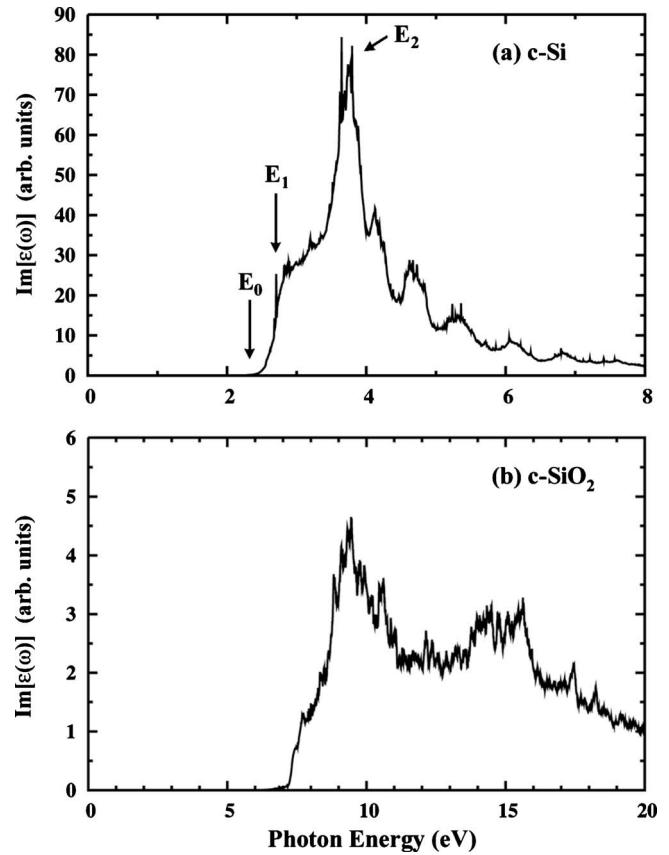

FIG. 6. Computed imaginary component of $\varepsilon(\omega)$ for both (a) c-Si and (b) c-SiO$_2$ (α-quartz phase). Unlike their amorphous counterparts, the spectra of crystalline materials reveal distinct peaks that are attributed to transitions near Van Hove singularities in the joint density of states. The nomenclature for labeling optical transition energies in tetrahedrally-bonded semiconductors is described in further detail by Yu and Cardona (Ref. 1).

rive film densities. Since optical characterization of thin films through ellipsometry requires accurate description of structural parameters (film thickness, surface roughness, and substrate interface quality),[50,51] the validity of these requisite assumptions is paramount to the extracted properties. Furthermore, they report $\pm 10\%$ error in the measurement of H content of their films.

The results of Rantzer et al.[51] on films grown by dc magnetron sputtering corroborate our assertion that a greater change in H content in a-Si:H films is required to observe the blueshift in the E_2 transition energy. They report a change of only 0.5% in E_2 transition energy when H content is increased from 8 to 10 at. % H. This amount of change is effectively noise considering the uncertainty inherent in their fitting methods. In addition, they report a reduction in E_2 peak magnitude of only 1.1% for the same composition change.

In order to better correlate the relationship between optical spectra and electronic structure as a function of composition, we show the E_g and ε_o of all sample structures studied in Fig. 7. Figure 7(a) shows a trend of reduction in ε_o as H content increases in a-Si:H; however, a trend in E_g with composition is not readily apparent. We believe that the variation
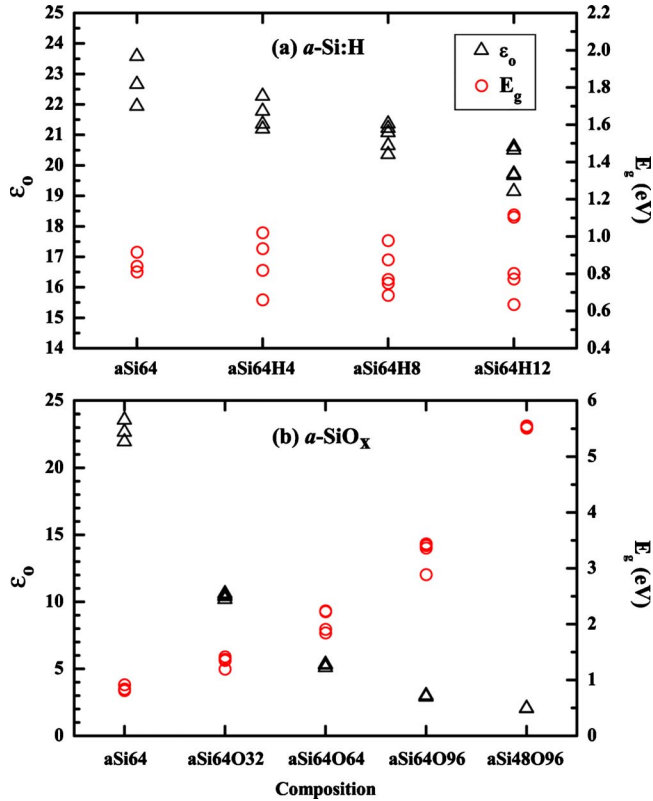
FIG. 7. (Color online) Dielectric constant (ε_o) and band gap (E_g) for all (a) a-Si:H and (b) a-SiO$_x$ amorphous structure samples studied. The dielectric constants were obtained from the optical spectra as $\lim_{\omega \to 0} \text{Re}[\varepsilon(\omega)]$. The band gaps were obtained from total density of states calculations for each sample. The data shown is produced from DFT-GGA calculations; therefore, E_g values are underestimated and ε_o values are overestimated. The scaling of ε_o and E_g in (a) was arbitrarily adjusted to separate the two trends for visual clarity.

in E_g observed is also aggravated by the aforementioned small increments in H composition across a-Si:H samples, which makes a clear trend difficult to resolve.

In addition, we analyzed supplemental simulation results which show that E_g generally decreases with sample mass density at an arbitrary a-Si:H composition, so fluctuations in density from sample-to-sample can produce small fluctuations in E_g, although these fluctuations in E_g are on the order of 0.01 eV. We suspect an increasing trend for E_g with increasing H content might be more apparent with larger supercells and/or increased sample sizes.

2. a-SiO$_x$

Similar to our a-Si:H optical response behavior, Fig. 5(a) shows the shape of $\text{Im}[\varepsilon(\omega)]$ incrementally transitions from a-Si to a-SiO$_2$ with a more pronounced trend than observed for a-Si:H. As O content increases, the magnitude of the E_2 absorption peak sharply decreases and blueshifts, while the absorption edge also blueshifts to higher photon energies. The decreasing peak magnitude with increasing O content is largely associated with an increasing band gap as shown in Fig. 7(b). As shown in Fig. 5(b), a similar incremental tran-

sition is evident in $\text{Re}[\varepsilon(\omega)]$ as O content increases from a-Si to a-SiO$_2$. Not only does the anomalous dispersion region blueshift, but the transition region also broadens in correlation with the peak broadening seen in the $\text{Im}[\varepsilon(\omega)]$ spectra. The incremental decrease in low-frequency ε_o ($\lim_{\omega \to 0} \text{Re}[\varepsilon(\omega)]$) is also evident in Fig. 5(b) as O content increases. The ε_o data obtained from each a-SiO$_x$ sample is consolidated as a function of composition in Fig. 7(b). Unlike the a-Si:H case, the inverse relationship between ε_o and E_g is vividly apparent over the complete a-SiO$_x$ composition range. Excellent precision is obtained across three samples for the predicted properties of a-SiO$_2$ as shown in Fig. 7(b).

Note that the DFT-GGA method employed here using the longitudinal form of the dielectric matrix provides instructive qualitative behavior for ε_o, but this method also tends to overestimate ε_o because the well-known band-gap underestimation increases ε_o, while lattice-constant sensitivity and finite basis-set errors have additionally been cited for inflating ε_o.[18,24] In addition, our values of ε_o reported are from the electronic contribution only, so no ionic contributions are considered. Previous studies have shown neglecting the ionic contribution will not change the trends observed, but can impact the magnitude of the ε_o values.[19] The work of Gajdoš et al.[24] provides more details on the sensitivity of the dielectric constant to various approximations within the PAW methodology used in our work.

For both the main absorption peak magnitude and ε_o, it is evident that the greatest changes occur for small values of x, when a-SiO$_x$ is most Si rich. This behavior is consistent with the semiempirical simulation study of Hübner[52] of semiconductor property variation in the transition region of c-Si/a-SiO$_2$ interfaces. In this study, various electronic properties, including valence charge-density distribution and band gap, are shown to have strong x variation for $0 \le x \le 1.5$, while properties become similar to a-SiO$_2$ for $x > 1.5$. In contrast to the conclusions of Hübner, we observe E_g [Fig. 7(b)] to increase more rapidly as x increases in a-SiO$_x$. In addition, we also observe the fundamental absorption edge to blueshift more rapidly for larger x [Fig. 5(a)]. We speculate that our results, particularly for E_g dependence on x, may differ from those of Hübner as a consequence of the crystalline structural models used. Not only is the $x=0$ structural contribution from c-Si by design (typical transistor substrate) in his study, but structural parameters derived from c-SiO$_2$ (β-cristobalite) are interpolated with x to model a-SiO$_x$ ($x > 0$). In contrast, our structures are all amorphous and bulk in nature.

Reliable optical property data in the literature is scarce for the intermediate compositions of a-SiO$_x$ ($0 \le x \le 2$), with only a limited amount of information for amorphous silicon monoxide. Hjortsberg and Granqvist[53] calculated $\varepsilon(\omega)$ of evaporated, 99%-pure a-SiO films using infrared spectrophotometric measurements. They report a static ε_o value of ~7.2 for a-SiO extracted from their $\text{Re}[\varepsilon(\omega)]$ spectra, while tabulated[54] optical properties for a-SiO suggest ε_o is 4.0. Our results from Fig. 7(b) produced an average ε_o for a-SiO of 5.3 across four samples. In our E_g data for the suboxide compositions, particularly aSi64O64 and aSi64O96, some spread in our computed values is attributable to a somewhat ambiguous band gap in which either or both the VB and CB

edges have a discontinuous splintering of eigenstates as a function of energy; as a result, it is not possible to precisely define the edges of the gap in those cases. From our experience, we believe that the wide variation reported in material properties for these suboxide systems is a result of significant uncertainty in both composition (including impurities) and sample morphology.

In general, the more subtle changes in optical spectra with composition for a-Si:H relative to a-SiO$_x$ is largely correlated with the magnitude of change in optical gaps as composition changes. Furthermore, aside from any chemical effects, the physical range of composition investigated is much smaller for a-Si:H (0 to 15.8 at. % H) than for a-SiO$_x$ (0 to 66.7 at. % O), so the impact on resulting optical spectra should be significantly greater for a-SiO$_x$. The gaps are 1.4 eV and ~9.0 eV for a-Si (Ref. [1]) and a-SiO$_2$,[55] respectively, so the a-SiO$_x$ spectra presented cover a gap change of ~7.6 eV; in contrast, a maximum gap of about 1.8 eV (Ref. [1]) can be achieved in a-Si:H, so the a-Si:H spectra presented cover a gap change somewhat smaller than the limiting case of 0.4 eV.

We have detailed both the limitations and strengths of DFT-based property predictions in amorphous materials. The most significant limitation in our mechanical property predictions is attainment of either a sufficiently large supercell or a sufficiently large sample size to adequately represent a random bond topology network. The significant limitations in optical property predictions are grounded in both the well-known band-gap underestimation associated with DFT calculations and the independent-particle approximation for optical transitions. The chief strength of our approach, provided realistic structural models are used, is representation of an exact stoichiometric composition and nanoscale morphology. Experimental property measurements are often clouded by accurate identification of the sample material because factors including deposition process and conditions, annealing procedure, measurement technique, film density, material homogeneity, sample purity, and surface roughness all potentially influence the material properties we have investigated.

IV. CONCLUSIONS

In summary, we employ DFT-based methods for predicting the mechanical and optical properties of variable-composition amorphous matrices (a-Si:H and a-SiO$_x$). A statistical sampling of total-energy data for eight different amorphous compositions was used to calculate elastic (Y)

and bulk (B) moduli using second-order numerical derivatives. Addition of H to a-Si monotonically reduces Y by 18.3% and B by 16.2% as H incorporation increases to 15.8 at. % H in a-Si:H. Similarly, addition of O to a-Si monotonically reduces Y by 35.0% and B by 38.3% as x increases to 2.0 in a-SiO$_x$. In both cases, the reduction in moduli strongly correlates with decreasing sample density and is largely related to the weakening of the rigid tetrahedral network in Si.

We utilize an established PAW methodology based on calculation of the longitudinal form of the dielectric matrix to compute optical spectra for the imaginary and real parts of the complex dielectric function, $\varepsilon(\omega)$. As H is added to a-Si, we observe the intensity of the main E_2 transition peak of Im$[\varepsilon(\omega)]$ to decay slowly, while the low-frequency dielectric constant (ε_o) extracted from Re$[\varepsilon(\omega)]$ simultaneously decreases by 12.3% as the H content increases to 15.8 at. %. If our study were extended to higher H content in a-Si:H, we anticipate that the expected blueshift in the E_2 transition peak with increasing H content would also become apparent. As O is added to a-Si, similar, but more pronounced, changes are seen in the optical spectra. A reduction in E_2 peak intensity is accompanied by a blueshift of both the E_2 transition energy and the fundamental absorption edge. Values of ε_o decrease by 91.0% as x increases to 2.0 in a-SiO$_x$. Unlike the a-Si:H case, the decrease in ε_o with increasing O content is observed to strongly correlate with the significant increase in E_g as x increases in a-SiO$_x$.

We have summarized the strengths and acknowledged the limitations in using DFT methods to predict mechanical and optical properties in amorphous materials. Considering the large variation in reported experimental measurements and the limited availability of previous computational results, our property predictions provide valuable insight into the mechanical and optical behavior of a-Si:H and a-SiO$_x$ materials, especially for the less-characterized intermediate compositions.

*Author to whom correspondence should be addressed; gshwang@che.utexas.edu

[1] P. Y. Yu and M. Cardona, *Fundamentals of Semiconductors* (Springer-Verlag, New York, 2001).

[2] R. Kuschnereit, H. Fath, A. A. Kolomenskii, M. Szabadi, and P. Hess, Appl. Phys. A **61**, 269 (1995).

[3] D. E. Carlson and C. R. Wronski, Appl. Phys. Lett. **28**, 671 (1976).

[4] D. L. Staebler and C. R. Wronski, Appl. Phys. Lett. **31**, 292 (1977).

[5] C. R. Wronski, B. von Roedern, and A. Kolodziej, Vacuum **82**, 1145 (2008).

[6] V. Beyer, J. von Borany, and M. Klimenkov, J. Appl. Phys. **101**, 094507 (2007).

[7] G. Gawlik and J. Jagielski, Nucl. Instrum. Methods Phys. Res. B **266**, 1307 (2008).

[8] G. A. Kachurin, S. G. Cherkova, D. V. Marin, R. A. Yankov, and M. Deustchmann, Nanotechnology **19**, 355305 (2008).

[9] D. Yu, S. Lee, and G. S. Hwang, J. Appl. Phys. **102**, 084309 (2007).

[10] J. P. Perdew and Y. Wang, Phys. Rev. B **45**, 13244 (1992).

[11] G. Kresse and J. Hafner, Phys. Rev. B **47**, 558 (1993); **49**, 14251 (1994); G. Kresse and J. Furthmüller, Comput. Mater. Sci. **6**, 15 (1996); Phys. Rev. B **54**, 11169 (1996).

[12] G. Kresse and J. Furthmüller, *VASP the Guide* (Vienna University of Technology, Vienna, 2001).

[13] D. Vanderbilt, Phys. Rev. B **41**, 7892 (1990).

[14] P. E. Blöchl, Phys. Rev. B **50**, 17953 (1994).

[15] M. J. Mehl, Phys. Rev. B **47**, 2493 (1993).

[16] F. Birch, J. Geophys. Res. **83**, 1257 (1978).

[17] W. F. Hosford, *Mechanical Behavior of Materials* (Cambridge University Press, New York, 2005).

[18] B. Adolph, J. Furthmüller, and F. Bechstedt, Phys. Rev. B **63**, 125108 (2001).

[19] I. J. Wu and G. Y. Guo, Phys. Rev. B **76**, 035343 (2007).

[20] K. Sánchez, I. Aguilera, P. Palacios, and P. Wahnón, Phys. Rev. B **79**, 165203 (2009).

[21] L. E. Ramos, E. Degoli, G. Cantele, S. Ossicini, D. Ninno, J. Furthmüller, and F. Bechstedt, Phys. Rev. B **78**, 235310 (2008).

[22] K. Seino, F. Bechstedt, and P. Kroll, Nanotechnology **20**, 135702 (2009).

[23] J. Furthmüller, http://www.freeware.vasp.de/VASP/optics, 2009.

[24] M. Gajdoš, K. Hummer, G. Kresse, J. Furthmüller, and F. Bechstedt, Phys. Rev. B **73**, 045112 (2006).

[25] G. Y. Guo, K. C. Chu, D.-S. Wang, and C.-G. Duan, Phys. Rev. B **69**, 205416 (2004).

[26] Y.-N. Xu and W. Y. Ching, Phys. Rev. B **44**, 11048 (1991).

[27] K. Tanaka, E. Maruyama, T. Shimada, and H. Okamoto, *Amorphous Silicon* (Wiley, Chichester, England, 1999).

[28] I. N. Levine, *Physical Chemistry* (McGraw-Hill, St. Louis, Missouri, 1995).

[29] J. Sarnthein, A. Pasquarello, and R. Car, Phys. Rev. B **52**, 12690 (1995).

[30] F. Mauri, A. Pasquarello, B. G. Pfrommer, Y.-G. Yoon, and S. G. Louie, Phys. Rev. B **62**, R4786 (2000).

[31] M. Szabadi, P. Hess, A. J. Kellock, H. Coufal, and J. E. E. Baglin, Phys. Rev. B **58**, 8941 (1998).

[32] A. Brunet-Bruneau, D. Souche, S. Fisson, V. Nguyen Van, G. Vuye, F. Abeles, and J. Rivory, J. Vac. Sci. Technol. A **16**, 2281 (1998).

[33] K. Jarolimek, R. A. de Groot, G. A de Wijs, and M. Zeman, Phys. Rev. B **79**, 155206 (2009).

[34] X. Jiang, B. Goranchev, K. Schmidt, P. Grünberg, and K. Reichelt, J. Appl. Phys. **67**, 6772 (1990).

[35] W. A. Brantley, J. Appl. Phys. **44**, 534 (1973).

[36] Bulk modulus was computed from tabulated experimental values of Y and ν from Ref. 31 using $B = Y/[3(1-2\nu)]$.

[37] K. Tanaka, Solid State Commun. **60**, 295 (1986).

[38] V. Kulikovsky, V. Vorlicek, P. Bohac, M. Stranyanek, R. Ctvrtlik, and A. Kurdyumov, Thin Solid Films **516**, 5368 (2008).

[39] T. Rouxel, J. Am. Ceram. Soc. **90**, 3019 (2007).

[40] *Handbook of Nanotechnology*, edited by B. Bhushan (Spring-Verlag, New York, 2004).

[41] H. Ni, X. Li, and H. Gao, Appl. Phys. Lett. **88**, 043108 (2006).

[42] X. Li, B. Bhushan, K. Takashima, C.-W. Baek, and Y.-K. Kim, Ultramicroscopy **97**, 481 (2003).

[43] V. I. Ivashchenko, P. E. A. Turchi, and V. I. Shevchenko, Phys. Rev. B **75**, 085209 (2007).

[44] P. Kroll, J. Non-Cryst. Solids **345-346**, 720 (2004).

[45] R. W. Hoffman, Jr., T. E. Mitchell, and R. W. Hoffman, Thin Solid Films **154**, 149 (1987).

[46] *Properties of Amorphous Silicon and its Alloys*, edited by T. Searle (INSPEC, London, 1998).

[47] R. B. Sosman, *The Properties of Silica* (Chemical Catalog, New York, 1927).

[48] T. Otobe, K. Yabana, and J.-I. Iwata, J. Phys.: Condens. Matter **21**, 064224 (2009).

[49] G. F. Feng, M. Katiyar, J. R. Abelson, and N. Maley, Phys. Rev. B **45**, 9103 (1992).

[50] D. A. G. Bruggeman, Ann. Phys. **416**, 636 (1935).

[51] A. Rantzer, H. Arwin, J. Birch, B. Hjörvarsson, J. W. P. Bakker, and K. Järrendahl, Thin Solid Films **394**, 255 (2001).

[52] K. Hübner, J. Non-Cryst. Solids **35-36**, 1011 (1980).

[53] A. Hjortsberg and C. G. Granqvist, Appl. Opt. **19**, 1694 (1980).

[54] *Handbook of Optical Constants of Solids*, edited by E. D. Palik (Academic Press, San Diego, CA, 1997).

[55] T. Koslowski, W. Kob, and K. Vollmayr, Phys. Rev. B **56**, 9469 (1997).